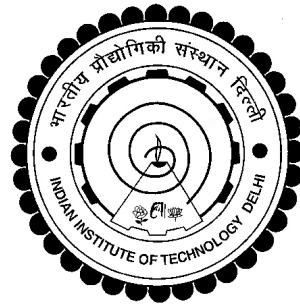


NUMERICAL INVESTIGATION OF
THREE-DIMENSIONAL TRANSITION IN THE WAKE
OF A HEATED SQUARE CYLINDER

MOHD PERWEZ ALI



DEPARTMENT OF APPLIED MECHANICS
INDIAN INSTITUTE OF TECHNOLOGY DELHI
MARCH 2026

© Indian Institute of Technology Delhi (IITD), New Delhi, 2026

NUMERICAL INVESTIGATION OF
THREE-DIMENSIONAL TRANSITION IN THE WAKE
OF A HEATED SQUARE CYLINDER

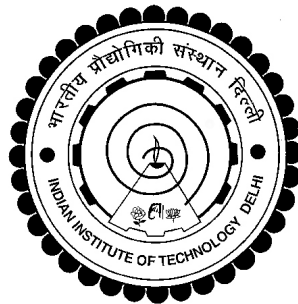
by

MOHD PERWEZ ALI

Department of Applied Mechanics

Submitted

in fulfillment of the requirements of the degree of Doctor of Philosophy
to the



INDIAN INSTITUTE OF TECHNOLOGY DELHI

MARCH 2026

Certificate

This is to certify that the thesis entitled “**Numerical investigation of three-dimensional transition in the wake of a heated square cylinder**”, being submitted by **Mohd Perwez Ali** to the Indian Institute of Technology Delhi for the award of the degree of **Doctor of Philosophy**, is a record of the bonafide research carried out by him which has been prepared under our supervisions in conformity with the rules and regulations of the Indian Institute of Technology Delhi. The research reports and results presented in the thesis has not been submitted for any degree or diploma in any other university or institute.

Prof. Sanjeev Sanghi

Department of Applied Mechanics
Indian Institute of Technology Delhi
New Delhi - 110016
India

Prof. Nadeem Hasan

Department of Mechanical Engineering
ZHCET, Aligarh Muslim University
Aligarh - 202002
India

Acknowledgments

All praise be to Almighty ALLAH for His countless blessings and for granting me the strength, patience, and capability to pursue and complete this doctoral research journey.

I express my deepest gratitude to my supervisors, Prof. Sanjeev Sanghi and Prof. Nadeem Hasan, for their invaluable mentorship, insightful suggestions, and constant encouragement throughout the course of my PhD. Their guidance has played a pivotal role in shaping the direction and quality of this research. I am also thankful to the members of my Student Research Committee (SRC), Prof. Amitabh Bhattacharya, Prof. Anupam Dewan, and Prof. Amit Gupta, for their constructive feedback, thoughtful discussions, and encouragement during various stages of this work. I would also like to acknowledge Prof. Faisal S. Baig, whose course on Computational Fluid Dynamics (CFD) during my M.Tech program laid a strong foundation for my coding skills.

I am also grateful for the computational resources provided by the High Performance Computing (HPC) facility at the Indian Institute of Technology Delhi, which enabled the extensive simulations required for this work. Furthermore, I extend sincere thanks to all the members of the CFD Laboratory for their technical support, stimulating discussions, and for maintaining a motivating research environment. Lastly, I remain deeply indebted to my family for their unconditional support, sacrifices, and prayers. Their patience, encouragement, and faith in me have been my strongest source of motivation throughout this journey.

MOHD PERWEZ ALI

Abstract

This thesis presents a comprehensive direct numerical simulation (DNS) study of three-dimensional transitions in the wake of an infinitely long heated square cylinder, modeled using a spanwise periodic computational domain, subjected to uniform cross-flow of air (Prandtl number, $Pr = 0.7$) in the presence of thermal buoyancy. A non-Oberbeck–Boussinesq (NOB) compressible flow model is employed to account for variations in thermophysical and transport properties under large-scale heating conditions. To solve the governing compressible flow equations, a variant of the flux-based Particle Velocity Upwind-Modified (PVU-M+) scheme is utilized, employing finite difference techniques. A low Mach number of $M = 0.1$ is used to minimize pressure compressibility effects. The amount of heating is controlled by the overheat ratio, expressed as $\varepsilon = (T_w - T_\infty)/T_\infty$, where T_w is the wall temperature and T_∞ is the free-stream temperature.

At a Reynolds number of $Re = 250$, the heated wake exhibits multiple three-dimensional instability modes as heating increases. These modes are characterized by changes in the number of streamwise vortex pairs and the associated spanwise wavelength λ_z/L , where L denotes the side length of the square cylinder. As the heating level increases, the shorter wavelength structure Mode-B ($\lambda_z/L \sim 1.2$), observed in the unheated cylinder wake, transitions to longer wavelength structures: Mode-E ($\lambda_z/L \sim 2$) and Mode-D ($\lambda_z/L \sim 3$). The emergence and suppression of vortex dislocations are closely associated with the heating intensity, thereby influencing the unsteady force characteristics and frequency spectra.

A detailed analysis at $Re = 180$ highlights the role of baroclinic vorticity production

and thermophysical property variations in wake behavior. The chaotic wake associated with Mode-A instability in the unheated case transitions into a two-dimensional wake at low heating levels ($\varepsilon = 0.2$), followed by the emergence of periodic and quasi-periodic three-dimensional wakes as the heating level increases. The streamwise baroclinic vorticity production term (Γ_x) is identified as a key contributor to the generation of streamwise vorticity (Ω_x), while the spanwise term (Γ_z) plays an indirect role in redistributing rotational energy among other vorticity components, thereby modulating vortex shedding strength and frequency.

At $Re = 300$, the effect of free-stream orientation on the wake dynamics of the heated cylinder is investigated. Under aiding buoyancy, increasing heat input results in the suppression of vortex shedding and the development of steady or quasi-steady plume-like structures. In contrast, cross-buoyancy induces more complex and asymmetric wake behavior characterized by sustained vortex shedding. The imbalance between positively and negatively signed baroclinic term Γ_z introduces asymmetry in the wake, contributing to negative (downward) lift generation and an earlier onset of vortex shedding. The competing influences of the baroclinic terms Γ_x and Γ_z govern the degree of wake three-dimensionality, exhibiting distinct mechanisms across buoyancy configurations. Under aiding buoyancy, Γ_z suppresses vortex shedding and consequently weakens three-dimensionality. Conversely, in the cross-buoyancy case, the stronger Γ_x enhances the Ω_x , promoting increased three-dimensionality despite the presence of suppressive effects from Γ_z .

Finally, the evolution of wake instability modes is examined for a heated cylinder in cross-flow configuration under large-scale heating ($\varepsilon = 1.0$) across a Reynolds number range of $Re = 50$ to 300 . A critical Reynolds number of $Re_{cr} = 113$ is identified for the onset of three-dimensional flow. Four distinct instability modes (such as Mode-D, Mode-E, Mode-DD*, and Mode-D*) are observed, each corresponding to a specific Reynolds number range. These mode transitions are characterized by both gradual and abrupt variations in the Strouhal number–Reynolds number ($St-Re$) relationship. Vortex

dislocations are found to significantly influence the wake structure and associated hydrodynamic forces. Additionally, the study establishes that a periodic spanwise domain length of $H_z = 6L$ is sufficient to resolve all relevant wake features with both qualitative and quantitative accuracy.

सारांश

यह शोध प्रबंध एक अनंत लंबाई वाले तापित वर्गाकार सिलेंडर के पीछे वेक में त्रि-आयामी संक्रमणों का एक व्यापक प्रत्यक्ष संख्यात्मक अनुकरण (DNS) अध्ययन प्रस्तुत करता है, जिसे स्पैनवाइज़ आवर्त संगणनात्मक क्षेत्र का उपयोग करके मॉडल किया गया है, और जो तापीय उछाल की उपस्थिति में वायु के समान अनुप्रस्थ प्रवाह (प्रेण्ड्टल संख्या, $Pr = 0.7$) के अधीन होता है। बड़े पैमाने के तापन की स्थितियों में ऊष्मीय-भौतिक तथा परिवहन गुणों में होने वाले परिवर्तनों को ध्यान में रखने के लिए एक गैर-ओबरबेक-बूसिनेस्क (NOB) संपीड्य प्रवाह मॉडल का उपयोग किया गया है। शासकीय संपीड्य प्रवाह समीकरणों को हल करने के लिए फ्लक्स-आधारित पार्टिकल वेलोसिटी अपविड-संशोधित (PVU-M+) स्कीम का एक रूपांतर, फाइनाइट डिफरेंस तकनीकों का उपयोग करते हुए अपनाया गया है। दाब संपीड्यता प्रभावों को न्यूनतम करने के लिए $M = 0.1$ की निम्न मैक संख्या का उपयोग किया गया है। तापन की मात्रा को ओवरहीट अनुपात $\varepsilon = (T_w - T_\infty)/T_\infty$ द्वारा नियंत्रित किया जाता है, जहाँ T_w दीवार का तापमान है और T_∞ मुक्त प्रवाह का तापमान है।

रेनॉल्ड्स संख्या $Re = 250$ पर, तापित वेक तापन बढ़ने के साथ अनेक त्रि-आयामी अस्थिरता मोड प्रदर्शित करता है। इन मोडों की विशेषता स्ट्रीमवाइज़ भंवर युग्मों की संख्या तथा संबंधित स्पैनवाइज़ तरंगदैर्घ्य λ_z/L में परिवर्तन द्वारा होती है, जहाँ L वर्गाकार सिलेंडर की भुजा की लंबाई को निरूपित करता है। जैसे-जैसे तापन स्तर बढ़ता है, बिना तापन वाले सिलेंडर वेक में देखी जाने वाली छोटी तरंगदैर्घ्य संरचना Mode-B ($\lambda_z/L \sim 1.2$) लंबी तरंगदैर्घ्य संरचनाओं Mode-E ($\lambda_z/L \sim 2$) और Mode-D ($\lambda_z/L \sim 3$) में परिवर्तित हो जाती है। भंवर विस्थापन (vortex dislocations) का उद्भव और दमन तापन की तीव्रता से घनिष्ठ रूप से संबंधित है, जिससे अस्थिर बल विशेषताओं और आवृत्ति स्पेक्ट्रा प्रभावित होते हैं।

$Re = 180$ पर एक विस्तृत विश्लेषण वेक व्यवहार में बैरोक्लिनिक भंवरता उत्पादन तथा ऊष्मीय-भौतिक गुणों में परिवर्तन की भूमिका को उजागर करता है। बिना तापन के मामले में Mode-A अस्थिरता से संबंधित अराजक वेक कम तापन स्तर ($\varepsilon = 0.2$) पर एक द्वि-आयामी वेक में परिवर्तित हो जाता है, जिसके बाद तापन स्तर बढ़ने पर आवर्ती तथा अर्ध-आवर्ती त्रि-आयामी वेक का उद्भव होता है। स्ट्रीमवाइज़ बैरोक्लिनिक भंवरता उत्पादन पद (Γ_x) को स्ट्रीमवाइज़

भंवरता (Ω_x) के उत्पादन में एक प्रमुख योगदानकर्ता के रूप में पहचाना गया है, जबकि स्पैनवाइज़ पद (Γ_z) अन्य भंवरता अवयवों के बीच घूर्णन ऊर्जा के पुनर्वितरण में अप्रत्यक्ष भूमिका निभाता है, जिससे भंवर शेडिंग की तीव्रता और आवृत्ति नियंत्रित होती है।

$Re = 300$ पर, मुक्त प्रवाह अभिविन्यास का तापित सिलेंडर के वेक गतिकी पर प्रभाव का अध्ययन किया गया है। सहायक उछाल (aiding buoyancy) के अंतर्गत, तापन इनपुट बढ़ने पर भंवर शेडिंग का दमन होता है और स्थिर या अर्ध-स्थिर प्लूम-जैसी संरचनाओं का विकास होता है। इसके विपरीत, क्रॉस-उछाल (cross-buoyancy) अधिक जटिल और असममित वेक व्यवहार उत्पन्न करता है, जिसकी विशेषता निरंतर भंवर शेडिंग है। धनात्मक तथा ऋणात्मक चिह्नित बैरोक्लिनिक पद Γ_z के बीच असंतुलन वेक में असममितता उत्पन्न करता है, जो ऋणात्मक (नीचे की ओर) लिफ्ट उत्पन्न करने और भंवर शेडिंग के शीघ्र आरंभ में योगदान देता है। बैरोक्लिनिक पदों Γ_x और Γ_z के प्रतिस्पर्धी प्रभाव वेक की त्रि-आयामीता की मात्रा को नियंत्रित करते हैं तथा विभिन्न उछाल विन्यासों में भिन्न तंत्र प्रदर्शित करते हैं। सहायक उछाल के अंतर्गत, Γ_z भंवर शेडिंग को दबाता है और परिणामस्वरूप त्रि-आयामीता को कमजोर करता है। इसके विपरीत, क्रॉस-उछाल के मामले में, अधिक प्रबल Γ_x , Ω_x को बढ़ाता है, जिससे Γ_z के दमनकारी प्रभावों की उपस्थिति के बावजूद त्रि-आयामीता में वृद्धि होती है।

अंततः, बड़े पैमाने के तापन ($\varepsilon = 1.0$) के अंतर्गत क्रॉस-फ्लो विन्यास में तापित सिलेंडर के लिए वेक अस्थिरता मोडों के विकास का अध्ययन $Re = 50$ से 300 की रेनॉल्ड्स संख्या सीमा में किया गया है। त्रि-आयामी प्रवाह की शुरुआत के लिए $Re_{cr} = 113$ की एक क्रांतिक रेनॉल्ड्स संख्या की पहचान की गई है। चार विशिष्ट अस्थिरता मोड (जैसे Mode-D, Mode-E, Mode-DD*, और Mode-D*) देखे गए हैं, जिनमें से प्रत्येक एक विशिष्ट रेनॉल्ड्स संख्या सीमा के अनुरूप है। ये मोड संक्रमण स्ट्रुहल संख्या-रेनॉल्ड्स संख्या ($St-Re$) संबंध में क्रमिक तथा आकस्मिक दोनों प्रकार के परिवर्तनों द्वारा विशेषीकृत हैं। भंवर विस्थापन वेक संरचना तथा संबंधित जलगतिकीय बलों को महत्वपूर्ण रूप से प्रभावित करते हैं। इसके अतिरिक्त, अध्ययन यह स्थापित करता है कि $H_z = 6L$ की एक आवर्त स्पैनवाइज़ डोमेन लंबाई सभी प्रासंगिक वेक विशेषताओं को गुणात्मक तथा मात्रात्मक दोनों दृष्टियों से सटीक रूप से निरूपित करने के लिए पर्याप्त है।

Contents

Certificate	i
Acknowledgments	iii
Abstract	v
Contents	xi
List of Figures	xv
List of Tables	xxiii
Nomenclature	xxv
1 Introduction	1
1.1 Motivation	1
1.2 Historical background	3
1.3 Literature review	5
1.3.1 Three-dimensional instability modes in the isothermal wake . . .	5
1.3.2 Physical mechanisms of Mode-A and Mode-B instabilities	8
1.3.3 Vortex dislocations in the isothermal wake	9
1.3.4 Flow regimes in wake transition of a heated cylinder	11
1.3.5 Wake transition flow in the presence of aiding buoyancy	11
1.3.6 Wake transition flow in the presence of cross-buoyancy	13

1.3.7	Conclusion from the literature	15
1.4	Problem description	16
1.5	Objectives of the thesis	18
1.6	Organization of the thesis	19
2	Computational methodology	21
2.1	Governing equations	21
2.1.1	Governing equations in body-fitted coordinates	26
2.2	Computational grid generation	26
2.3	Initial and boundary conditions	28
2.4	Model validation	30
2.4.1	$St - Re$ and $\overline{C}_D - Re$ characteristics	30
2.4.2	Tongue-shaped and rib-like vortical structure	34
2.5	Summary	35
3	Effect of heating on wake structures and flow parameters	37
3.1	Vortical structures in the wake of a square cylinder	38
3.2	Time-averaged velocity and temperature fields	43
3.3	Temporal variation of global parameters	45
3.4	Vortex shedding frequency	50
3.5	Spatiotemporal average of spanwise surface vorticity and local Nusselt number	51
3.6	Summary	52
4	Influence of baroclinic vorticity production and effective thermophysical properties on the wake dynamics	55
4.1	Wake bifurcation to Mode-E instability	56
4.2	Chaotic, periodic, and quasi-periodic behavior of wake	58
4.3	Time-averaged pressure field and streamlines pattern	62

4.4	Baroclinic vorticity production	64
4.5	Translational and rotational energy dynamics	66
4.6	Spanwise vorticity in the near wake	68
4.7	Effective thermophysical properties	69
4.8	Lift coefficient and frequency spectra	72
4.9	Summary	75
5	Impact of aiding and cross-buoyancy on wake three-dimensionality and vortex shedding	77
5.1	Three-dimensional wake structures	78
5.2	Time histories of drag and lift coefficients	82
5.3	Vortex dislocations	85
5.4	Vortex shedding	88
5.5	Intermittent vortex shedding in the presence of aiding buoyancy at $\varepsilon = 0.4$	92
5.6	Wake three-dimensionality and rotational energy norms	94
5.7	Symmetric and asymmetric flow pattern	97
5.8	Summary and discussion	100
6	Identification of three-dimensional wake instability mode regimes at large-scale heating	103
6.1	Three-dimensional instability modes	104
6.2	The Strouhal-Reynolds number relationship	106
6.3	Impact of vortex dislocations on wake dynamics	108
6.4	Dependency of wake instabilities on periodic span length	110
6.5	Summary	114
7	Conclusions and future work	117
7.1	Effects of heating on 3-D spatio-temporal flow structures in a cross-flow configuration at $Re = 250$	118

7.2	Impact of baroclinic vorticity production and thermophysical property variations on wake dynamics at $Re = 180$	119
7.3	Role of baroclinic vorticity production in wake dynamics for aiding and cross-flow configurations at $Re = 300$	121
7.4	Reynolds number dependence of 3-D wake modes in the large-scale heating regime under cross-flow configuration	122
7.5	Scope for further study	124
Appendices		125
A Numerical scheme		125
A.1	Particle Velocity Upwind-Flux Intercell (PVU-FI) scheme	127
A.2	Comparison of PVU-M+ and PVU-FI schemes for flow around a square cylinder	129
A.2.1	Streamwise vortical structures	129
A.2.2	Flow field in vicinity of the square cylinder	131
A.2.3	Fluctuations in force coefficients and frequency spectra	133
B Domain and grid independence studies		137
Bibliography		143

List of Figures

1.1	A periodic span length H_z of an infinitely long square cylinder subjected to a free-stream crossflow (U_∞, T_∞) inclined at an angle α relative to gravity \vec{g} .	16
2.1	A two-dimensional O -type body-fitted mesh around a square cylinder in ξ, η coordinates within the $x - y$ plane shown in (a) an enlarged view and (b) a magnified view near the corner.	27
2.2	The present values of two-dimensional (2-D) and three-dimensional (3-D) wake transitions at $\varepsilon = 0.0$ and $M = 0.1$ compared with the reported values obtained using various methodologies showing in the plots of (a) $St - Re$ and (b) $\overline{C}_D - Re$	31
2.3	Iso-contours of Ω_x in the isothermal wake of a square cylinder at $\varepsilon = 0.0$ and $M = 0.1$, showing (a) the tongue-shaped vortical structure with longer wavelength of Mode-A instability at $t = 400$ for $Re = 180$, and (b) the rib-like vortical structure with shorter wavelength of the Mode-B instability at $t = 300$ for $Re = 250$. The blue and light yellow color represent positive and negative vortices, respectively.	34
3.1	The vortical structure (visualized using the Q-criterion and colored by Ω_x) in the wake of a square cylinder at $Re = 250$ and $t = 1700$ for (a) $\varepsilon = 0.0$, (b) $\varepsilon = 0.4$, and (c) $\varepsilon = 1.0$	39

3.2	Contours of streamwise vorticity at $Re = 250$ showing spanwise wavelength (λ_z/L) in the wake of a square cylinder at $x = 7$ for (a) $\varepsilon = 0.0$, (b) $\varepsilon = 0.2$, (c) $\varepsilon = 0.4$, (d) $\varepsilon = 0.6$, (e) $\varepsilon = 0.8$, and (f) $\varepsilon = 1.0$	40
3.3	Side view of the wake structure (visualized using the Q-criterion and colored by Ω_z) behind a square cylinder at $Re = 250$ and $t = 1700$ for (a) $\varepsilon = 0.0$, (b) $\varepsilon = 0.4$, (c) $\varepsilon = 0.6$ and (d) $\varepsilon = 1.0$	42
3.4	Contours of the time-averaged velocity magnitude at $Re = 250$, exhibiting the variation of the velocity field around a square cylinder for (a) $\varepsilon = 0.0$, (b) $\varepsilon = 0.2$, (c) $\varepsilon = 0.4$, (d) $\varepsilon = 0.6$, (e) $\varepsilon = 0.8$, and (f) $\varepsilon = 1.0$	43
3.5	Contours of the time-averaged temperature field at $Re = 250$ displayed in the wake of a square cylinder for (a) $\varepsilon = 0.0$, (b) $\varepsilon = 0.2$, (c) $\varepsilon = 0.4$, (d) $\varepsilon = 0.6$, (e) $\varepsilon = 0.8$, and (f) $\varepsilon = 1.0$	44
3.6	Time histories of the drag coefficient (C_D) at $Re = 250$ for heating levels (a) $\varepsilon = 0.0$, (b) $\varepsilon = 0.4$, and (c) $\varepsilon = 1.0$	46
3.7	Time histories of the lift coefficient (C_L) at $Re = 250$ for heating levels (a) $\varepsilon = 0.0$, (b) $\varepsilon = 0.4$, and (c) $\varepsilon = 1.0$	47
3.8	Time histories of the Nusselt number (Nu) at $Re = 250$ for heating values (a) $\varepsilon = 0.0$, (b) $\varepsilon = 0.4$, and (c) $\varepsilon = 1.0$	47
3.9	At $Re = 250$, the temporal variation of global parameters with varying levels of heating for $t = 1900 - 1930$ shown in plots of (a) C_D , (b) C_L , and (c) Nu	48
3.10	(a) The frequency spectra of C_L shown at various heating levels for $Re = 250$. (b) The variation in the value of Strouhal number (St) with increase in heating level.	50
3.11	The spatiotemporal average of spanwise surface vorticity and the local Nusselt number of a heated square for various heating levels at $Re = 250$ shown in the plots of (a) $\overline{\overline{\Omega_{zs}}} - \xi$ and (b) $\overline{\overline{Nu_s}} - \xi$. Here A, B, C, and D represent the sharp corners of a square cylinder.	51

4.1	The vortical structure (Q-criterion) in a square cylinder wake colored by Ω_x at $Re = 180$ and $t = 1300$ for (a) $\varepsilon = 0.0$, (b) $\varepsilon = 0.2$, (c) $\varepsilon = 0.4$, (d) $\varepsilon = 0.6$, (e) $\varepsilon = 0.8$, and (f) $\varepsilon = 1.0$	57
4.2	Time history of spanwise velocity (w) in a square cylinder wake ($x = 2$, $y = 0$, $z = 3$) at $Re = 180$ and $M = 0.1$ for $\varepsilon = 0.0 - 1.0$	59
4.3	The wake behavior of a square cylinder at $Re = 180$ and $M = 0.1$ for various heating levels ($\varepsilon = 0.0 - 1.0$) shown by (a) spanwise velocity (w) located at the near-wake ($x = 2$, $y = 0$, $z = 3$), and its (b) frequency spectra, f	60
4.4	Time-averaged pressure field of a fully developed flow in the mid-plane ($z = 3$) around a square cylinder at $Re = 180$ and $M = 0.1$ for (a) $\varepsilon = 0.0$, (b) $\varepsilon = 0.2$, (c) $\varepsilon = 0.6$, and (d) $\varepsilon = 1.0$	62
4.5	Time-averaged streamlines pattern (colored by velocity magnitude) of a fully developed flow shown in the mid-plane ($z = 3$) of a square cylinder at $Re = 180$ and $M = 0.1$ for (a) $\varepsilon = 0.0$, (b) $\varepsilon = 0.6$, and (c) $\varepsilon = 1.0$	63
4.6	Iso-surfaces at $t = 1300$ of positive (brown) and negative (light yellow) streamwise baroclinic vorticity $\Gamma_x = \pm 0.05$ in a square cylinder wake at $Re = 180$ and $M = 0.1$ for (a) $\varepsilon = 0.4$, (b) $\varepsilon = 0.6$, (c) $\varepsilon = 0.8$, and (d) $\varepsilon = 1.0$	65
4.7	Spatial distribution of Ω_z (a,c,e) and Γ_z (b,d,f) in the wake of the mid-span of a heated square cylinder at $Re = 180$ for $\varepsilon = 0.2$, 0.6 , and 1.0	68
4.8	The changes in thermophysical and transport properties of fluid particles with increasing heating level at $Re = 180$ and $M = 0.1$ around a square cylinder within radial distances of $5L$, $15L$, and $25L$ shown in the plots of (a) $\mu_{eff} - \varepsilon$, (b) $\kappa_{eff} - \varepsilon$, (c) $\rho_{eff} - \varepsilon$, (d) $C_{veff} - \varepsilon$, (e) $Pr_{eff} - \varepsilon$, and (f) $Re_{eff} - \varepsilon$	70

4.9	(a) Temporal variation of C_L , and (b) a close view of onset of three-dimensionality in a small time interval, shown at $Re = 180$ and $M = 0.1$ for $\varepsilon = 0.0 - 1.0$	73
4.10	Frequency spectra of C_L at $Re = 180$ for $\varepsilon = 0.0 - 1.0$	74
5.1	Isosurfaces of streamwise vorticity (Ω_y) at $Re = 300$ and $t = 1500$ showing rib-like (a), braid-like (b) and tube-like (c-e) vortical structures with distinct vortex pairs across varying heating levels under aiding buoyancy ($\alpha = 0^\circ$). The magnitude of these vortex structures diminishes as heating levels rise, with yellow indicating positive values and blue indicating negative values.	79
5.2	Isosurfaces of streamwise vorticity (Ω_x) at $t = 1900$ showing disordered rib-like vortical structures with distinct vortex pairs in the presence of cross-buoyancy ($\alpha = 90^\circ$) for (a) $\varepsilon = 0$, (b) $\varepsilon = 0.3$, (c) $\varepsilon = 0.6$ and (d) $\varepsilon = 1.0$. The growing magnitude of these vortical structures with increasing ε values suggests a strengthening of wake three-dimensionality. Yellow and blue colors represent positive and negative values, respectively.	80
5.3	Time histories of C_D and C_L presented at $Re = 300$ under aiding buoyancy ($\alpha = 0^\circ$) for increasing heating levels $\varepsilon = 0$ (a1,a2), $\varepsilon = 0.2$ (b1,b2), $\varepsilon = 0.4$ (c1,c2), and $\varepsilon = 0.6$ (d1,d2). The progressive decrease in the amplitudes of C_D and C_L with increasing ε indicates a weakening and eventual suppression of vortex shedding. The highlighted temporal signal at $\varepsilon = 0.2$ reveals the presence of large-scale vortex dislocations in the flow field.	83
5.4	Time histories of C_D and C_L at $Re = 300$ with cross-buoyancy ($\alpha = 90^\circ$) shown for various heating levels $\varepsilon = 0$ (a1,a2), $\varepsilon = 0.2$ (b1,b2), $\varepsilon = 0.6$ (c1,c2), and $\varepsilon = 1$ (d1,d2). The reduction in the mean C_L with increasing thermal input is attributed to the development of an asymmetric flow pattern.	84

5.5	The vortex dislocations in the flow field at $Re = 300$, $\varepsilon = 0.2$ and $\alpha = 0$ shown by irregularities in the temporal data of (a) transverse velocity u in the near wake at $(x = 2, y = 0, z = 3)$ and (b) lift coefficient C_L	86
5.6	Isosurfaces of Ω_z at distinct time instants illustrating ordered (b, d) and disordered (a, c) vortical structures for $Re = 300$, $\varepsilon = 0.2$, and $\alpha = 0$. Positive and negative values of Ω_z are represented by red and blue, respectively. The disruption of coherent structures by vortex dislocations leads to the emergence of disordered flow patterns.	87
5.7	Spatial distributions of Ω_z (a1,b1,c1,d1,e1) and Γ_z (a2,b2,c2,d2,e2) at $Re = 300$ shown for different values of ε under aiding buoyancy conditions ($\alpha = 0^\circ$). The generation of plume-like Γ_z structures with a sign opposite to that of Ω_z plays a significant role in weakening and suppressing vortex shedding in the cylinder wake.	89
5.8	Spatial distributions of Γ_z (a1,b1,c1) and Ω_z (a2,b2,c2) at $Re = 300$ shown for $\varepsilon = 0.2, 0.6$, and 1 under cross-buoyancy conditions ($\alpha = 90^\circ$). The production of exclusively positive Γ_z vortices on the upstream side ($-1 < x < 0.5$) within the boundary layers strengthens the positive Ω_z while weakening the negative Ω_z , leading to irregular and weakened vortex shedding in the cylinder wake.	90
5.9	Isosurfaces of $\Omega_y = \pm 0.2$ (a1,b1,c1,d1) and contours of Ω_z (a2,b2,c2,d2) shown at different time instants for $\varepsilon = 0.4$, $Re = 300$ and $\alpha = 0^\circ$. The braid-like structures are associated with weak vortex shedding, while the tube-like structures correspond the absence of shedding.	93
5.10	The time-averaged energy norms $\bar{E}(\Omega_x)$, $\bar{E}(\Omega_y)$, $\bar{E}(\Gamma_x)$ and $\bar{E}(\Gamma_z)$ with increasing ε values at $Re = 300$ shown for aiding buoyancy at $\alpha = 0^\circ$ (a,c,e) and cross-buoyancy at $\alpha = 90^\circ$ (b,d,f).	95

5.11	The strength of positive and negative vortices of Ω_z and Γ_z compared using their energy norms with increasing heating levels for aiding buoyancy at $\alpha = 0^\circ$ (a,c) and cross-buoyancy at $\alpha = 90^\circ$ (b,d).	98
6.1	Isosurfaces of vortical structures ($a1,b1,c1$) and contours of Ω_x ($a2,b2,c2$) at $\varepsilon = 1.0$, illustrating distinct wake instability modes at $Re = 140$ ($a1,a2$), $Re = 190$ ($b1,b2$), and $Re = 280$ ($c1,c2$). These instability modes such as Mode-D, Mode-E, and Mode-D* are classified based on the spanwise wavelength λ_z/L , estimated from Ω_x pair counts across the entire span. Isosurfaces are visualized using the Q -criterion and are colored by Ω_x . An asterisk (*) denotes a disordered vortical structure.	105
6.2	The $St - Re$ relationship for a heated square cylinder at $\varepsilon = 1.0$ showing distinct regimes of 3-D instability modes D, E, DD* and D*, each associated with specific Reynolds number ranges. The emergence of instability modes occurs through gradual and discontinuous changes in the $St - Re$ curve.	107
6.3	Iso-surfaces of streamwise vorticity ($\Omega_x = \pm 0.7$) at $Re = 205$ and $\varepsilon = 1.0$ across different time instants in the square cylinder wake, showing (a) Mode-D*, (b) Mode-D and (c) Mode-D*. Here, yellow and blue colors denote positive and negative values respectively.	108
6.4	The time-histories of spanwise velocity w (in the near wake at $x = 2$, $y = 0$, $z = 3$) and drag coefficient C_D observed at $Re = 205$ and $\varepsilon = 1.0$ for cylinder span-lengths of $H_z = 6L$ (a,c) and $H_z = 3L$ (b,d). The intermittent fluctuations shown in (a,c) for $H_z = 6L$ suggest the presence of vortex dislocations in the flow field, which are suppressed for $H_z = 3L$	109
6.5	Iso-surfaces of streamwise vorticity at $\varepsilon = 1.0$ shown for cylinder span-lengths of $H_z = 9L$, $6L$ and $3L$ at $Re = 130$ (a,c,e) and $Re = 205$ (b,d,f). Here, yellow and blue colors denote positive and negative values respectively.	111

6.6	The C_L spectra at $\varepsilon = 1.0$ for cylinder span-lengths $H_z = 6L$ and $H_z = 3L$ observed at $Re = 130$ ($a1, a2$), $Re = 205$ ($b1, b2$) and $Re = 210$ ($c1, c2$). The variation in the dominant vortex shedding frequency, i.e., the Strouhal number, is shown for both span lengths.	112
6.7	The time-averaged enstrophies at $\varepsilon = 1.0$, with the increase in periodic span length, shown in the $\mathcal{E} - H_z$ plots at (a) $Re = 130$ (Mode-D), (b) $Re = 205$ (Mode-DD*) and (c) $Re = 210$ (Mode-D*).	113
A.1	Iso-contours at $t = 500$ of positive (light yellow) and negative (blue) streamwise vorticity Ω_x with $M = 0.1$ and $M = 0.5$ for $Re = 250$ using PVU-M+ scheme (a,c) and PVU-FI scheme (b,d).	130
A.2	At $Re = 250$, pressure contours around the cylinder at mid-span ($z = 3$) for $M = 0.1$ and $M = 0.5$ using PVU-M+ scheme (a,c) and (b) PVU-FI scheme (b,d).	131
A.3	Transverse velocity (v) contours around the cylinder at mid-span ($z = 3$) for $M = 0.5$ and $Re = 250$ using (a) PVU-M+ scheme and (b) PVU-FI scheme.	132
A.4	For $Re = 500$ and $M = 2$, pressure contours around the cylinder at mid-span ($z = 3$) employing PVU-M+ and PVU-FI schemes with enlarged (a,b) and magnified view (c,d).	132
A.5	Time history of force coefficients for $M = 0.1$ and $Re = 250$ using PVU-M+ scheme (a,c) and PVU-FI scheme (b,d).	134
A.6	Frequency spectra of lift coefficients for $M = 0.1$ and $Re = 250$ using (a) PVU-M+ scheme and (b) PVU-FI scheme.	134
B.1	Profiles of $\overline{\overline{Nu_s}}$ at $Re = 500$ and $\varepsilon = 1.0$ for various meshes refined in (a) the $\xi - \eta$ plane and (b) z -direction. Here A, B, C, and D denote the sharp corners of a square cylinder.	141

List of Tables

1.1	The Re_{cr} and the corresponding spanwise wavelengths (λ_z/L) for Modes A and B, as observed across various studies employing different methodologies.	8
2.1	Boundary conditions for the various types of waves at inflow and outflow.	28
2.2	The variations in the values of Strouhal number (St) and time-averaged drag coefficient (C_D) with free-stream Mach number (M) at $Re = 250$. Source: Rolandi et al. (2023)	32
2.3	Comparison of the present numerical values of Re_{cr} and λ_z/D (for Mode-A and Mode-B) at $\varepsilon = 0.0$ with the values reported in previous studies for flow past an unheated square cylinder.	35
4.1	The transfer of time-averaged three-dimensional energy shown at $Re = 180$ in the form of translational and rotational energy norms for $\varepsilon = 0.0 - 1.0$.	67
5.1	The distinct shapes of vortical structures associated with varying Ω_y pairs at $Re = 300$ presented for ε values ranging from 0 to 1 under aiding buoyancy ($\alpha = 0^\circ$). The classification of instability modes is determined based on the spanwise wavelength (λ_z/L), which is calculated from the number of Ω_y vortex pairs observed over the total span length of $6L$.	79

5.2	Disordered rib-like vortical structures with varying Ω_x pairs presented at $Re = 300$ for increasing ε values under cross-buoyancy conditions ($\alpha = 90^\circ$). The distinct 3-D wake instability modes are designated based on their corresponding wavelength, with an asterisk (*) indicating disordered vortical structures.	81
6.1	The dependency of wake instability modes with the variation of periodic span lengths at $\varepsilon = 1.0$ listed for $Re = 130, 205$ and 210	110
7.1	The distinct instability modes at large-scale heating ($\varepsilon = 1$) presented over the Reynolds number range of $Re = 113$ to 300 . The classification of these modes is based on the spanwise wavelength (λ_z/L). An asterisk (*) denotes a disordered vortical structure.	123
B.1	Domain size independence check at $Re = 500$ and $\varepsilon = 1.0$	140
B.2	Grid refined in the $\xi - \eta$ plane at $Re = 500$ and $\varepsilon = 1.0$	140
B.3	Grid G2 refined in the $z-$ direction at $Re = 500$ and $\varepsilon = 1.0$	140

Nomenclature

Abbreviations

Symbol	Description
CFD	Computational Fluid Dynamics
DNS	Direct Numerical Simulation
HPC	High-Performance Computing
NOB	Non-Oberbeck–Boussinesq
MPI	Message Passing Interface
RMS	Root Mean Square

Notations

Symbol	Description
Re	Reynolds number
Re_{cr}	critical Reynolds number
Ri	Richardson number
Pr	Prandtl number
Fr	Froude number
M	Mach number
Nu	Nusselt number
St	Strouhal number
ρ_∞	free-stream density

p_∞	free-stream pressure
U_∞	free-stream velocity
T_∞	free-stream temperature
μ_∞	free-stream dynamic viscosity
ν_∞	free-stream kinematic viscosity
k_∞	free-stream thermal conductivity
t	dimensionless time
Δt	dimensionless time-step
ρ	dimensionless density
p	dimensionless pressure
μ	dimensionless dynamic viscosity
ν	dimensionless kinematic viscosity
k	dimensionless thermal conductivity
E	dimensionless total specific energy
C_v	dimensionless constant volume-specific heat
\vec{V}	dimensionless fluid velocity
V_N	dimensionless local normal velocity
V_T	dimensionless local tangential velocity
g	gravity
ε	overheat ratio
λ_z	spanwise wavelength
γ	specific heat ratio
β	thermal expansion coefficient
R_d	cylindrical domain radius
L	side length of the square cylinder
H_z	periodic span-length of square cylinder
T_w	uniform cylinder surface temperature
α	free-stream inclination angle relative to gravity

x, y, z	dimensionless Cartesian coordinates
u, v, w	dimensionless fluid velocity components along x, y, z directions
$\Omega_x, \Omega_y, \Omega_z$	vorticity along x, y, z directions
$\Gamma_x, \Gamma_y, \Gamma_z$	baroclinic vorticity production terms along x, y, z directions
ΔT	temperature difference between the cylinder surface and the free-stream
i, j, k	local indices
ξ, η	curvilinear coordinates
C_D	drag coefficient
C_L	lift coefficient
\bar{C}_D	time-averaged drag coefficient
\bar{C}_L	time-averaged lift coefficient
1-D	one-dimensional
2-D	two-dimensional
3-D	three-dimensional
∇	gradient operator
∇^2	laplace operator
∂	partial derivative
∂^2	partial double derivative

